Additive Manufacturing 62 (2023) 103398

Contents lists available at ScienceDirect

Additive Manufacturing

journal homepage: www.elsevier.com/locate/addma

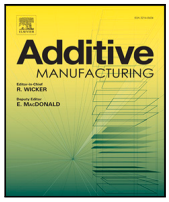

Research paper

Metal AM process-structure-property relational linkages using Gaussian process surrogates

Robert N. Saunders [a,b,*], Kirubel Teferra [a], Alaa Elwany [b], John G. Michopoulos [a], Dimitris Lagoudas [b]

[a] U.S. Naval Research Laboratory, Washington, 20375, DC, USA
[b] Texas A&M University, College Station, 77840, TX, USA

ARTICLE INFO

Keywords:
Process modeling
Microstructure
Mechanical properties
Stainless steel
Gaussian process

ABSTRACT

In metal additive manufacturing (AM), with sufficient understanding of process-structure–property (PSP) relational linkages, the control of build parameters can produce parts with previously unattainable properties. Establishing these PSP linkages involves varying process parameters until a desired microstructure, and corresponding properties, are achieved, either experimentally or computationally. However, both methods can have a high acquisition cost and be difficult to sample repeatedly. This work describes a Gaussian process (GP)-based workflow that is capable of predicting melt pool characteristics, microstructure features, and mechanical properties of previously unseen process parameter combinations. The workflow implements multi-fidelity, multi-output, and functional GPs, trained on a limited set of experiments and simulations in order to make melt pool, microstructure, and mechanical property predictions. The established linkage results in approximately 95% accuracy in predicting mechanical properties for previously unseen set of process parameters propagated through the whole framework. The use of GPs in the workflow limits the number of experiments/simulations needed, yields a nearly negligible cost for acquisition of new predictions, and allows for a Bayesian treatment of the PSP linkages that was not previously feasible.

1. Introduction

The repeated thermal cycling and high thermal gradients during metal additive manufacturing (AM) processes are known to result in microstructures that are vastly different from conventionally processed materials [1–3]. To adequately design, develop, and tailor the processed material to exhibit desired properties, and ultimately performance, for a targeted application, establishing process-structure–property (PSP) linkages is of utmost importance [4].

Establishing PSP linkages through experimental routes involves conducting intensive experimental campaigns (fabrication, characterization, and testing) over the entire processing parameter design space. The large parameter space along with the time consuming and expensive process of data collection greatly limits the number of samples that can be experimentally investigated [5]. One way to alleviate the intractability of those purely experimental methods is through predictive simulation capabilities aimed at quantifying PSP relations [6–8], including solidification modeling for process-structure (PS) relations [9] and mechanics of materials modeling for structure–property (SP) relations [10,11]. While these simulations are generally less costly than their experimental counterparts, they still pose considerable computational burdens, especially in the case of high-fidelity, multiscale simulations that provide the most physically consistent and accurate results. As a consequence of high computational costs, this class of simulations is not well suited for large scale parametric analyses involving processing parameter design space exploration, optimization and uncertainty quantification (UQ) [12] or problems in online, real time production updating [13].

Recent advances and accessibility of machine learning (ML) methods has made constructing, interpreting, and extracting information from experimental and simulation capabilities a relatively more tractable activity [14–18]. The process of applying ML, and more generally data science principles, to materials science and engineering is referred to as *materials informatics*.[19–22] Materials informatics principles provide the framework to streamline and accelerate the determination of process-structure (PS) [23], structure–property (SP) [24–26], and even full PSP [27] linkages in conventionally manufactured materials. ML is increasingly being used in AM applications [28–32], and the use of such tools for establishing PSP linkages is strongly

* U.S. Naval Research Laboratory, Washington, 20375, DC, USA.
E-mail address: robert.saunders@nrl.navy.mil (R.N. Saunders).

https://doi.org/10.1016/j.addma.2023.103398
Received 22 September 2022; Received in revised form 29 November 2022; Accepted 3 January 2023
Available online 5 January 2023
2214-8604/Published by Elsevier B.V.

motivated by the aforementioned large processing parameter design space [33–36]. While there is a growing body of work discussing the establishment of ML-based frameworks for PSP linkages in AM [7,37–39], to the authors' best knowledge only Wang et al. [40] have successfully demonstrated a full ML framework for PSP linkages in AM. In their work, the authors create Kriging surrogate models of thermal finite element (FE), phase field (PF), and fast Fourier transform crystal plasticity models then adjust those models using experiment data and propagate uncertainty through the surrogate models. The authors show a single demonstrative example using Ti-6Al-4V fabricated with selective electron beam melting (SEBM) of how uncertainty can propagate through the system and affect mechanical property predictions. While the authors demonstrate good validation scores for the thermal surrogate model, no information is presented about the accuracy of the microstructure and mechanical models. Likewise, no information is given about the number or type of experiments needed to tune the surrogate models.

The current study develops and demonstrates a complete PSP linkage in metal AM at the microscale by identifying physical simulation and experimental capabilities at each component of the linkage (*i.e.*, the process, structure, and properties), emulating each component of the linkage with a unique GP, then linking the GPs into a cohesive framework. GPs are chosen and implemented as they are ideally suited to operate with small data sets that will come from mechanistic models and experiments in AM [41]. The framework introduced in this work is demonstrated for laser powder bed fusion (L-PBF) processes using 316L stainless steel as a model material, although it is readily generalizable to other material systems. The remainder of the paper is structured as follows: Section 2 will briefly detail the GP-based surrogate models that form the foundation of the proposed framework to create the PSP linkage; Section 3 presents the results of each surrogate model training and validation; Section 4 links the trained surrogate models into a cohesive framework and shows results of the full PSP linkage on two test cases; Section 5 provides a discussion of the training and testing results, implications of the surrogate model-based PSP linkage, and potential improvements to the linkage; Finally, Section 6 summarizes the work and provides future research directions.

2. Methods

The PSP methodology consists of (1) a process model surrogate that relates process parameters to melt pool information by fusing information from multiple sources via a multifidelity GP (MFGP); (2) a process-structure (PS) surrogate that maps melt pool information to microstructure feature statistics through a multioutput GP (MOGP); and (3) a structure–property (SP) surrogate that maps microstructure feature statistics to microstructure mechanical properties, in the form of mesoscopic stress–strain curves, using a functional GP (fGP). The outputs of each surrogate model represent standard quantities of interest (QoIs) in AM that maintain congruence between physical models (*i.e.*, the output of one surrogate can serve as the input to the subsequent physical model or surrogate). Further discussion on the output selection for each surrogate model is detailed in the respective sections (Sections 2.1, 2.2, and 2.3). An overview of GPs is omitted here for brevity, but provided in Appendix along with brief details on the extensions to multifidelity, multioutput, and functional variants used in this work.

2.1. Process surrogate

The first step in understanding how the AM process parameters influence properties is to understand their effects on the thermal history during processing, and in particular, the geometry of the melt pool. There is a plethora of simulation and experiment capabilities focused on predicting the thermal history and corresponding melt pool geometry as functions of AM process parameters [42]. The MFGP A.1 is the proposed surrogate model for mapping processing parameters to features of the thermal history [43], because it can be generalized to incorporate any combination of simulation and experimental data. In the MFGP, multiple sources of information at varying degrees of fidelity can be incorporated into a single model. This limits the number of expensive simulations and/or experiments needed to build a model by leveraging information from cheap low fidelity solutions to the same problem. Though the MFGP uses a limited set of information at the highest fidelity, it is capable of producing a surrogate model that is as good as a standard GP model trained on a much larger set of high fidelity information alone. Therefore, the MFGP allows a high accuracy model to be obtained while significantly reducing the cost of acquisition of training data.

In this work, the MFGP is constructed based on information from, in ascending order of fidelity (*i.e.*, complexity and cost to generate simulations), the analytical solution of Eager and Tsai (ET) [44], the Naval Research Laboratory (NRL) enriched analytical solution method (NEASM) [45,46], an advective Eulerian heat transfer finite element (FE) model implemented in COMSOL, and L-PBF single track experiments (EXP) [47]. Each information source considers L-PBF melting of 316L stainless steel and 3 processing parameters: the laser power (P), velocity (V), and spot size (S)[1]. Due to the high acquisition cost of the higher fidelity information and limitations of the lowest fidelity model, only single-track data are considered. Information from all four fidelities is used to train the MFGP model in this work. Note that extensions to multiple tracks/layers are possible and will be discussed further in Section 5.

While simulations compute the full temperature field (*e.g.*, Fig. 1(a)) from which quantities of interest (*e.g.*, solidification rate/gradient, temperature gradient, cooling rate, *etc.*) can be extracted, experimental data are limited to quantities that are observable through available characterization techniques. Thus, melt pool dimensions (length (L), width (W), and depth (D)) are obtained from the simulations by extracting the domain enclosed by the melt temperature iso-surface. From the experiments, melt pool width and depth were extracted using optical microscopy (Fig. 1(b)). However, the melt pool length is unable to be obtained from the optical micrographs. Therefore, the MFGP model to predict L only uses information from the ET, NEASM, and FE simulations while the W and D predictions are based on all the simulation and experimental data. The workflow of the MFGP as described is shown in the diagram of Fig. 1(c).

2.1.1. Data sampling

In the case of a single fidelity data source, data is typically generated via a space-filling design of experiments (DoE) method such as latin hypercube sampling (LHS). However, simply sampling each of the fidelities used here from the different fidelities would result in multiple space filling designs that would not be nested and violate the assumptions of the MFGP. In order to ensure that the designs are nested, the scheme of Le Gratiet et al. [48,49] is chosen, where a space filling LHS design is created for the highest fidelity then repeated for each lower fidelity with each design in the next lowest fidelity being recursively adjusted to contain the points from the higher fidelities. For this work, the ET model is sampled 500 times, the NEASM sampled 200 times, FE sampled 100 times, and EXP sampled 50 times. The bounds for each fidelity DoE are the same and based on ranges of the AM experimental testbed. The minimum and maximum ranges for velocity, power, and spot size are 10–7000 mm/s, 75–400 W, and 50–350 μm, respectively. For training, all data are used except 15 experiments, which were randomly selected from the 50 available and used for validation of the trained MFGP. Cross-validation is not conducted for the MFGP as it requires iterative training of the model, which would be prohibitively costly given that the MFGP implemented already requires iterative training for each fidelity.

[1] More specifically, spot size is used to denote the distance equivalent to four standard deviations of a Gaussian beam profile, commonly referred to as D4σ

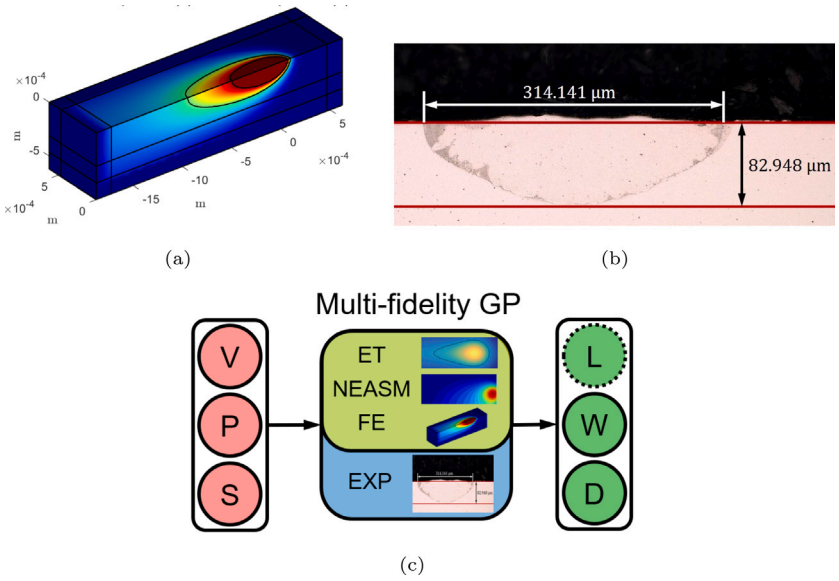

Fig. 1. MFGP representative outputs and workflow for creating the process modeling surrogate. (a) Representative single-track simulation output with temperature field shown [43]. (b) Representative transverse cross section of resolidified melt pool with corresponding dimensions [43]. (c) Diagram of the process surrogate linking process parameters to melt pool dimensions. The dashed line around the melt pool length output L is used to indicate that it is experimentally unobservable.

2.2. Process-structure surrogate

This link to relate process to structure is of great interest to the AM community. As stated earlier, AM microstructure can be vastly different from conventional microstructures and many existing microstructure reconstruction/feature extraction methods [23,50–52] may not be applicable. Popova et al. [53] recently developed a PS linkage for AM microstructures generated by kinetic Monte Carlo (kMC) methods using an ML workflow and spatial correlation methods. The workflow presented in [53] is quite general and is implemented in this work albeit with a different ML methodology and microstructure generation method.

In this work, a cellular automata finite element (CAFE) model is used that was introduced in Teferra and Rowenhorst [54]. The CAFE model takes processing parameters and melt pool dimensions as input and simulates solidification based on empirical thermally driven dendritic growth laws. The CAFE formulation for AM (e.g., [54–57]) is a medium fidelity model that sits between the kinetic Monte Carlo model (*e.g.*, [58–60]), and the phase field (*e.g.*, [61–66]) in terms of incorporation of the kinetics associated with solidification modeling. Its modeling of the competitive growth process arising from the interplay of preferential growth directions of dendrites having varying orientations with respect to the thermal gradient field along with thermally driven nucleation captures the dominant mechanisms of solidification. Further, it can simulate the large representative volume elements (RVEs) necessary to capture the microstructural feature statistics. The CAFE model used in this work has been validated for L-PBF 316L in terms of grain morphology and crystallographic texture as compared to electron backscatter diffraction (EBSD) characterization data. For more details, the readers are referred to Ref. [54].

The PS linkage is established by constructing an MOGP A.2 surrogate model that maps parameters described above to represent the melt pool (i.e., L, W, D) to statistical properties of microstructural features. The microstructure features are extracted from the CAFE model and selected such that the chosen outputs are the quantities needed for the subsequent linkage simulations and/or surrogate model. Thus, each set of generated parameters (*i.e.*, each sample in the training data set) are taken as input conditions to the CAFE model to generate representative volume element (RVE) solidified microstructures. Simultaneously, the constructed MFGP process surrogate maps these processing parameters to the parameters representing the melt pool, and the MOGP surrogate is constructed to map the output of the MFGP to statistical properties of selected microstructural features. A diagram of this linkage is shown in Fig. 2. The microstructural features include 7 morphology parameters: grain volume (V), 3 radii (r_1, r_2, and r_3) of the equivalent ellipsoid of a grain, and 3 orientation angles (ϕ, θ, and ψ) describing the rotation of this equivalent ellipsoid with respect to a reference axis; 3 additional parameters are include to describe the grain size and shape dependent constitutive model response: grain yield strength (g), initial strain hardening modulus (h), and grain boundary resistance (γ). The equivalent ellipsoid to a grain is set as the ellipsoid that matches the second moment of inertia properties of the grain [67].

Following the workflow and notation in Popova et al. [53], in the data preprocessing stage, the output microstructures from the CAFE model are augmented by removing the base plate and disregarding simulations that did not result in complete melting. Next, in the microstructure quantification stage, the RVEs for each CAFE simulation are processed to extract the 10 necessary parameter distributions. In this process, each grain in each simulation is represented by an equivalent ellipsoid via a linear least squares approach that results in the 7 morphology parameters for that grain. The additional constitutive model parameters are derived by numerically integrating material constants and an assumed grain boundary over the determined equivalent ellipsoid [68]. These 10 parameters are extracted for all grains in each RVE and then for each RVE that was simulated. This results in $\boldsymbol{Y}$ (Eq. (A.8)) having dimensions of $n_{samples} \times 10$, where the number of samples $n_{samples}$ is the number of RVEs that were simulated and used for training, and each of the 10 dimensions is a distribution of microstructure feature data for the given RVE. Next, the each of the 10 distributions of grain features from all $n_{samples}$ are merged into 10 unified distribution for each grain feature so that the dimensionality reduction stage can begin. A quantile transformer is applied to each unified grain feature distributions to obtain a fitted, reversible transformation process. A quantile transformer is a transformation that maps data from a given quantile in an arbitrary distribution to the corresponding quantile in a Normal distribution. That transformation process is then applied to each of the $n_{samples}$ RVEs so that from each RVE, 10 mean values and 10 variances can be obtained. This then results in $\boldsymbol{Y}$ having dimensions of $n_{samples} \times 20$, where each of the 20 outputs is now a scalar, rather than a distribution. However, this is a large number of outputs. To simplify the problem further, the outputs are reduced from 20 to 4 using principal component analysis.

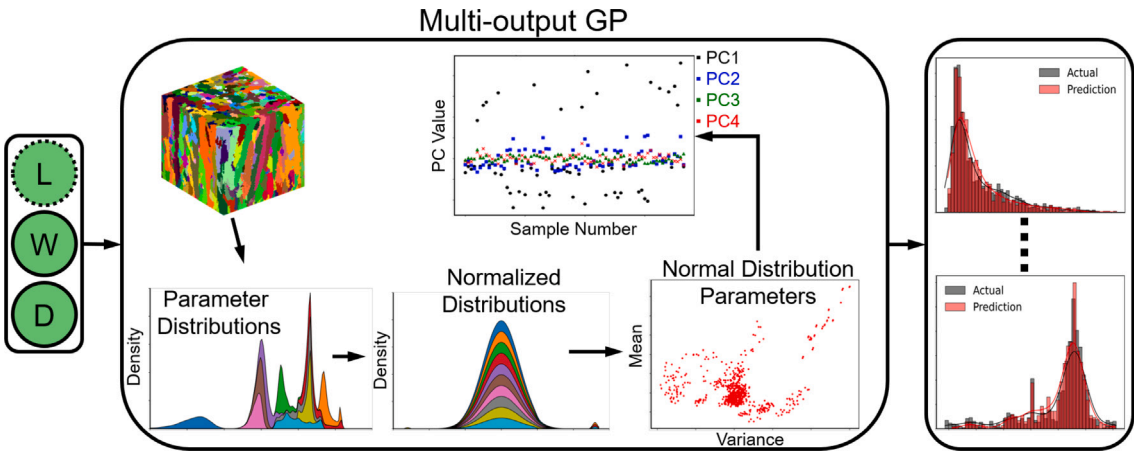

Fig. 2. Diagram of the process-structure surrogate linking melt pool information, in this case dimensions of length (L), width (W), and depth (D), to microstructure statistics such as grain volumes and orientations. Note that graph axes in the workflow are purposefully omitted as exact values vary with every sample microstructure and the graphs here are purely representative.

Using 4 components captures ≈99% of the variance of the underlying data for this problem. By examining the eigenvectors corresponding to each of the 4 PCs, it was observed that each PC contributes to all the 20 variables input into the PCA. This reflects the large amount of correlation among the 20 variables as indicative of the fact that ≈99% of the variance is found in 4 PCs. Thus, no direct relationship relating a PC to a physical microstructural feature or mechanical property can be obtained. The next stage in the process is the data-driven model estimation. In this stage, the MOGP is fitted to the training data.

The training data consists of 75 CAFE model generated RVEs, each having a unique generating set of melt pool dimensions and corresponding process parameters. Each CAFE model consists of a base plate, upon which 4 layers are printed with each layer containing 3 scans. Note that the base plate grains are omitted (described above) when extracting the features of the microstructure. The hatch spacing per simulation is set such that the melt pools associated with adjacent scans overlap according to the proportion described in Zhang et al. [69]. This approach ensures that there are no unmelted regions in the domain over the course of the simulation. Within a layer, the scans alternate directions (*i.e.*, a back and forth scan pattern), and the scan direction is rotated 90° layer-by-layer. Validation of the MOGP is accomplished by way of 10-fold cross-validation and a single left out test case that was randomly selected from the training data and was not used for training. As mentioned above, the MOGP utilized in this work assumes independent outputs, rather than coupled. This comes as a result of using principal components to represent the hyperparameters (*i.e.*, mean and variance) of the data and the Gaussian nature of the joint MOGP output distributions. Since the joint distribution is Gaussian, the principal components are, by definition, uncoupled (*i.e.*, uncorrelated and independent).

2.3. Structure–property surrogate

The SP surrogate in this work is based on the framework established by Saunders et al. [68] and is shown in Fig. 3. In this framework, microstructure RVEs are simulated using a microstructural-informed phenomenological crystal plasticity FE model. The input to each of these simulations are the 10 microstructure feature distributions described in the previous section along with a loading parameter (to drive displacement) and constitutive model parameters, which are fixed for a given material system (*i.e.*, 316L stainless steel for this work). From each simulation, mechanical properties in the form of grain stress and strain histories are extracted. By aggregating these histories for all grains in multiple simulations (with different microstructures having different features), two fGPs can be trained; one to predict a grain strain function and the other to predict a grain stress function given a set of grain features. Thus, given a new RVE, 10 microstructure features can be extracted for each grain in the RVE and a prediction of mechanical properties can be made for each grain. The predicted grain responses are then homogenized to make a prediction for the whole microstructure mechanical properties. For brevity, further discussion is omitted and the interested reader is referred to Ref. [68]. This framework is largely unmodified from its original development, but has been retrained using microstructures generated by the CAFE model described in Fig. 2. The simulated CAFE microstructures are more representative of real AM microstructures and demonstrate more realistic features than were in the previous training data.

3. Training & validation

For each of the surrogates established above, training and inference are performed in Python 3.6.12 using a mix of custom functions and standard libraries. Each of the GP models is trained using maximum likelihood estimation (MLE) to obtain hyperparameter estimates and each model is evaluated using the mean absolute percent error (MAPE). Training and validation results are first shown for each surrogate followed in the subsequent section by an application of the full PSP linkage.

3.1. Process surrogate

A separate MFGP is trained for each melt pool dimension (*i.e.*, length, width, and depth) to relate them to the input process parameters. Each of the three MFGPs trained is trained using information from all four fidelities discussed in Section 2.1. The MFGP trained on melt pool length is not discussed as there is no means to assess its predictive accuracy. This issue will be addressed in a future work. The trained MFGP prediction errors for the test set data are shown in Tables 1 and 2. Both mean absolute percent error (MAPE) and coefficient of determination (R^2) are shown. MAPE is formulated in such a way that it can sometimes result in erroneous, infinite, or undefined values and, as such, R^2 is implemented as an additional metric to verify the MAPE values seen are not erroneous and indicate that the data are not being overfit by the model. For comparison, a standard GP was trained on the available experiments, which results in a significantly worse model. Note that standard GPs were also trained using the other fidelities and resulted in worse models than the one trained using experiments alone as well as the MFGP. Additionally, it has been assumed that if experiments (*i.e.*, the ground truth) is available then they should be used in constructing any model, hence the most

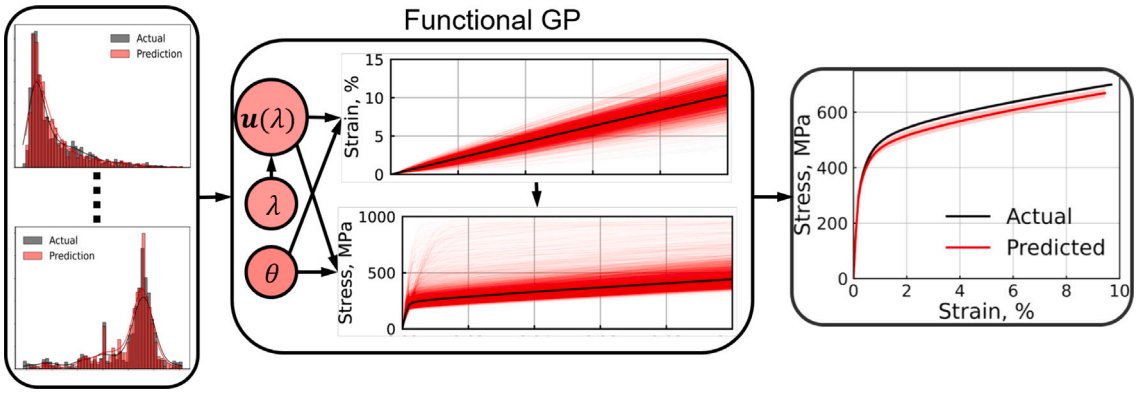

Fig. 3. Diagram of the structure–property surrogate linking microstructure statistics (distributions show representative predicted outputs of Fig. 2) to mechanical properties. The fGP takes microstructure statistics along with a loading parameter (λ) to drive displacement ($\boldsymbol{u}$) and constitutive model parameters (θ) to predict strain and then stress.

Table 1
Melt pool width and depth MAPE on the withheld test set data for the MFGP and a standard GP using only experiment data.

MAPE (%)	MFGP	GP
Width	4.5	11.9
Depth	11.5	33.7

Table 2
Melt pool width and depth R^2 on the withheld test set data for the MFGP and a standard GP using only experiment data.

R^2	MFGP	GP
Width	0.991	0.847
Depth	0.848	0.324

pertinent comparison is the one between the MFGP and the GP trained using experiments.

In addition to the test set average error metrics in Tables 1 and 2, parity plots are shown in Fig. 4. Note that the number of test data points between the width and depth models varies slightly due to the way in which the models were trained. The width model was evaluated on all available data, whereas the depth model was evaluated on screened data from test points that do not produce a porosity defect. For further details, the interested reader is referred to Saunders et al. [43]. From the parity plots, it can be seen that the MFGP has the intended effect of reducing the error for individual data points, while also reducing the associated variance. The reduction in error is also apparent in Table 1, where the use of the MFPG compared to a standard GP reduces error by over a factor of 2. Similar results are seen when examining R^2 values, which are significantly better when the MFGP is implemented.

3.2. Process-structure surrogate

The MOGP has the primary purpose of relating process parameters and melt pool dimensions to a set of 4 principal components that can be used to describe microstructure feature statistics. The process parameters used to determine the necessary melt pool dimensions to input into the MOGP are taken from the same training data as the MFGP. As such, the process surrogate training data and the MFGP predictions at these process parameters are equivalent due to the deterministic nature of GP predictions at training data locations. The 10-fold cross-validation results of the trained MOGP are shown in Fig. 5 with the explained variance ratio (EVR) (*i.e.*, the eigenvalue of that component normalized by the sum of all eigenvalues) of each PC shown. The CV results overall follow the 1:1 predicted:actual ratio that is ideal. The exception being the 3rd PC which is shows a constant predicted value of approximately 0.

Using the trained MOGP surrogate, the inputs for the randomly selected test case are propagated through the model to predict the 4 principal components of the microstructural features, which are then projected back (by performing the transformation described in Section 2.2) to obtain corresponding predictions for the 10 microstructural feature distributions. Fig. 6 shows the predicted and true probability density functions of the 3 radii of the equivalent ellipsoids representing grain morphology. For brevity, probability density functions of the remaining 7 features are not shown. From these histograms and corresponding kernel density estimates, it can be seen that the predicted distributions have some differences from the actual but, qualitatively, they are similar.

To assess quantitatively how similar the predicted and actual distributions are, the Kullback–Leibler (KL) divergence is applied to each of the microstructure features to assess the distance between the predicted and actual distributions. Ideally, the KL divergence is 0 for identical distributions, but it is not reasonable to expect that random samples from a predicted distribution or unobservable actual distribution would result in a 0 divergence. To determine what a reasonable value is for each feature, the KL divergence for all training/validation will be computed using the trained model, the cross-validated model, and the test case. Due to the deterministic nature of GPs, applying the trained model to the training data should result in perfect accuracy of the principal components and assess only the divergence induced by the transformation process. The KL divergence results are shown in Fig. 7. Box plots are shown to aggregate the information for each of the 74 cases from the training data using for training and cross-validation.

The first comparison that can be made for the KL divergence is that the results using the trained model to predict the training data and the cross-validation results are very similar for all microstructure features. This indicates that predicted principal component values of Fig. 5 are overall accurate and can reproduce the mean and variance values that originally went into the principal component analysis. Thus for new predictions, it is expected that the KL divergence should be similar to the values seen in Fig. 7. Additionally, the KL divergence results indicate that deviations from 0, especially for the trained model on the training data which is a deterministic prediction, are a result of the transformation process alone and demonstrate which microstructure feature transforms may need to be improved. Examining the test case shows expected behavior for the KL divergence in that the divergence of the test case is in the same range as the cross-validation results.

In addition to the KL divergence, the first two moments of the microstructure feature distributions were computed for the 74 training cases and 1 test case. This was done to establish if the relative divergence values computed were reasonable in an absolute sense. As with the data in Fig. 7, the moments were computed on the training data with the trained model, the cross-validation data, and the test case. In general, the first moment showed an average absolute error

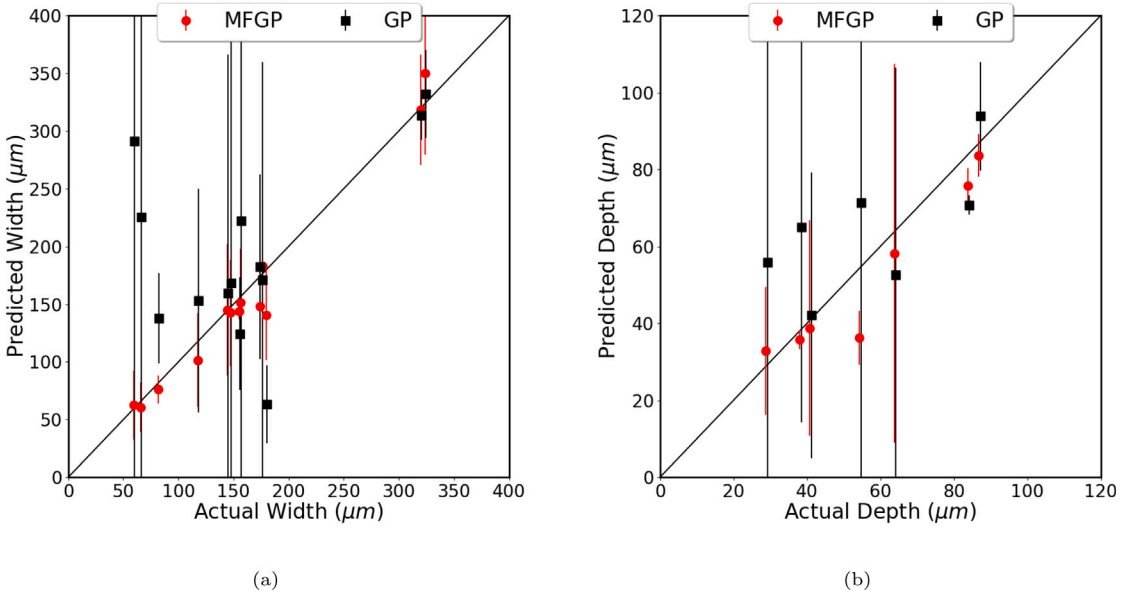

Fig. 4. Parity plots for the withheld test set data using the MFGP and standard GP using only experiment data : (a) melt pool width, (b) melt pool depth.

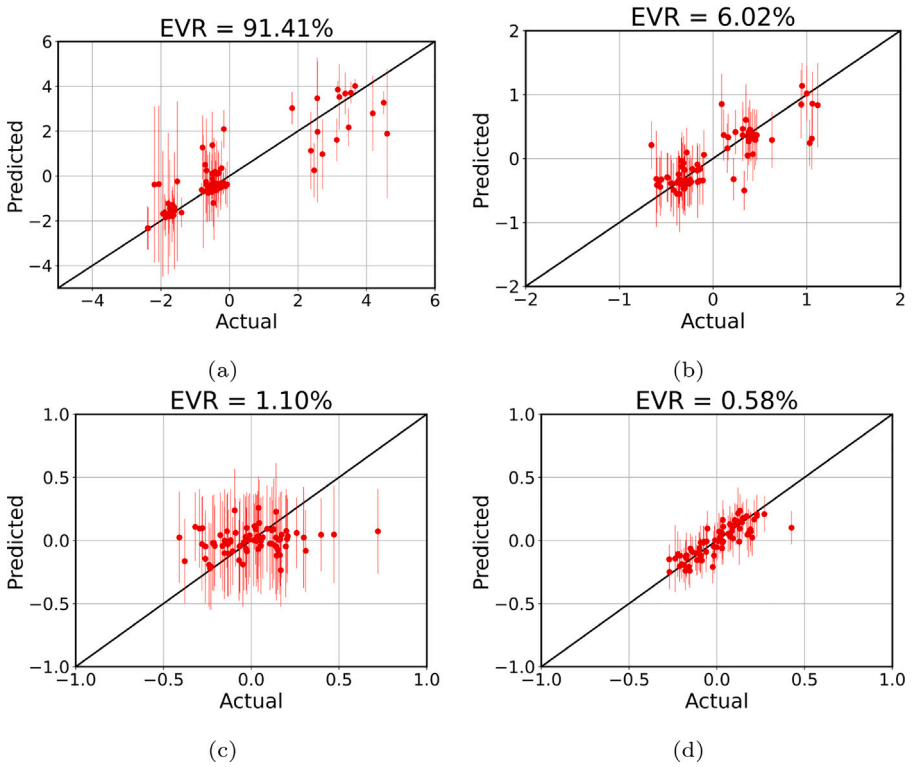

Fig. 5. 10-fold cross-validation parity plots for the dominant 4 principal component of the microstructural features comparing the MOGP surrogate prediction with the training data: (a) 1st PC, (b) 2nd PC, (c) 3rd PC, (d) 4th PC. The explained variance ratio (EVR) is shown above each plot.

of ≈10% with the second moment having average absolute errors in the 10%–20% range for all 10 features. These ranges hold on the training, cross-validation, and test data. Taken in conjunction with the qualitatively good results, this demonstrates that the MOGP is able to approximately reproduce the microstructure features.

3.3. Structure–property surrogate

As mentioned the fGP framework that makes up the SP surrogate is largely unmodified in this work with the exception that it is trained on the CAFE model data generated to create the PS surrogate. The results of this retraining are shown in Fig. 8 and in Table 3. Note that error bounds shown in this and all subsequent fGP predictions are the 95% predicted GP confidence interval and do not account for uncertainty from all surrogate models. Two comparisons are used to evaluate the efficacy of the retrained model. First, a test set that consisted of 30% of the available training data that contains a range of microstructure features representative of the entire feature space, and second, a CAFE model microstructure that was originally shown in the supplement of [68], which was not used to retrain the fGPs and was generated

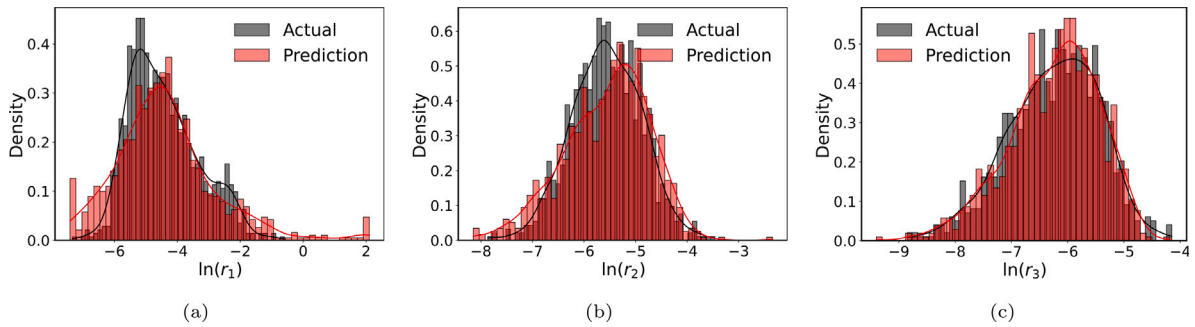

Fig. 6. Predicted versus actual probability density functions of the equivalent ellipsoidal radii for the test case: (a) ellipsoid major axis radius, (b) ellipsoid intermediate axis radius, (c) ellipsoid minor axis radius. The natural log of the radii is shown.

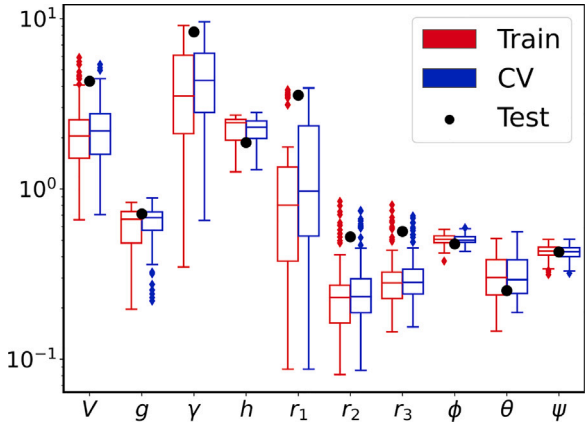

Fig. 7. Kullback–Leibler divergence for each of the microstructure features for the trained model predicting the training data, cross-validation (CV) data, and test case.

Table 3
MAPE for the fGP strain and stress predictions on the withheld test data set and previously unseen CAFE model microstructure.

MAPE (%)	Test data	CAFE data
Strain	0.698	3.91
Stress	2.41	3.41

using a different scan pattern and process parameters than the training data. Note that the use of a test set that has been withheld during training of the fGP is demonstrative of the average error that would be obtained on any new microstructure RVE. Additionally, since the withheld data consist of features over the entire space, accuracy on that set is more representative of the true model error, more so than any single microstructure RVE with a limited range of features would be.

The fGP models both demonstrate a high accuracy on the test data as well as the previously unseen CAFE microstructure. On average, the fGPs tends to slightly overpredict stress and strain on the test data. Likewise, the fGPs predict the mechanical properties of the CAFE microstructure with under 4% error. Note, that the error rate achieved without retraining was approximately 30% for strain and 17% for stress. Interestingly, this happens even though the scan pattern and process parameters used to generate the microstructure were different than the patterns and parameters used in the training set. This indicates that there may be some level of agnosticism in the structure–property surrogate with regard to how the AM microstructure is generated.

Table 4
MAPE for the predicted properties using the CAFE model microstructure (CAFE-fGP) and the MOGP microstructure feature output distributions of the same microstructure (MOGP-fGP). The errors are quantified near the yield point, at the final increment, and over the whole curve.

MAPE (%)	CAFE-fGP		MOGP-fGP	
	Strain	Stress	Strain	Stress
≈1% Strain (Yield)	2.25	6.02	6.05	4.47
Final increment	0.514	3.73	3.68	3.83
Overall	1.12	4.91	4.72	4.38

4. PSP surrogate linkage

4.1. MOGP-fGP linkage

As a first test of the developed surrogate models and their linkages, the left out test case from the MOGP (Section 3.2) is propagated through SP linkage. Both the actual microstructure statistics and the MOGP predicted statistics are input to the SP linkage. The output of this process along with the CAFE microstructure used to generate the data is shown in Fig. 9 with errors quantified in Table 4. The first point that can be made is that the CAFE-CPFE (*i.e.*, the true value) requires approximately 36 h on a high performance computing (HPC) system using 144 CPUs in parallel. In contrast, the CAFE-fGP solution requires approximately 8 h, with the vast majority of the time and resources being used to run the CAFE model, and the MOGP-fGP solution takes only a couple minutes using a single CPU on a laptop. Next, it can be seen from Fig. 9 that the predicted stress–strain curves for both the CAFE-based microstructure statistics and MOGP-based microstructure statistics are very similar to the physics-based model outputs. The CAFE seems to over-predict while the MOGP seems to under-predict.

Examining the average error over the curve (*i.e.*, the percent difference between the elements in each curve) shows that, in fact, the predicted curves are all qualitatively and quantitatively similar. The error in predicted strain for the CAFE-fGP is approximately 1% and approximately 5% for the MOGP-fGP case. The predicted stress error for both is around 4–5%. This indicates that with only a small penalty in error, which is to be expected with any predictive model, an orders of magnitude reduction in computational time and resources is possible.

4.2. PSP linkage

To further examine the points made above and extend the predictions to include the MFGP melt pool dimension predictions, two new sets of process parameters are chosen from the withheld MFGP test cases and propagated through the full PSP linkage. These cases correspond to process parameters (P, V, S) of (10 W, 100 mm/s, 300 μm) for test case 1 and (600 W, 300 mm/s, 160 μm) for test case 2. These two cases represent a good set of points as they are far from each

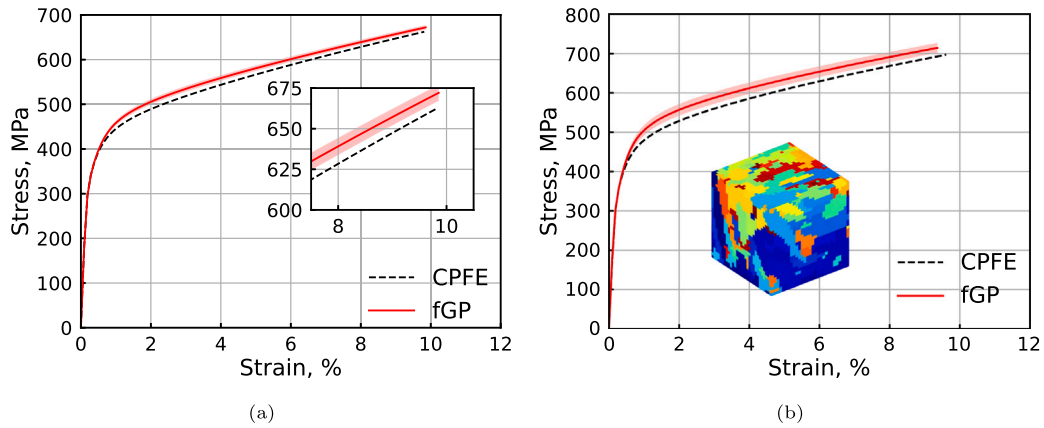

Fig. 8. fGP network predictions for withheld test data and a withheld CAFE microstructure after retraining using CAFE model microstructures of Section 2.2. (a) Average response of withheld data after retraining. (b) Predicted response of a CAFE RVE after retraining.

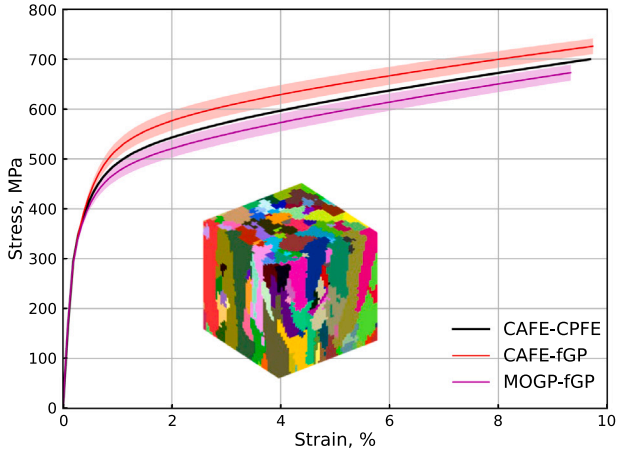

Fig. 9. MOGP test case predicted properties compared to physics-based modeling properties with 95% GP predicted confidence interval.

other in terms of the process space. Case 1 is a low power, slow, wide beam whereas case 2 is a more focused, higher power, faster beam. For case 1, this set of parameters is close to a regime of where lack of fusion defects may occur, and for case 2, the parameters are close to the keyholing defect regime. In both cases, experiment images shows that a melt pool was formed and did not exhibit keyholing or lack of fusion defects. It is imperative to note here that these process parameters have been completely unseen during the training of all surrogates and their propagation through the entire framework is demonstrative of how this framework could perform in a real-world scenario where multiple sets of parameters are being weighed against one another.

From these inputs, the process model surrogate is queried and the corresponding predictions for melt pool width and depth are shown in Table 5. The prediction error rates of 5% and 9.5% for the width and depth, respectively, are similar to the validation set errors discussed in Section 3.1, as one would expect. The predicted and actual values can now be used as input to both the CAFE and MOGP models. Since experiment melt pool length is unavailable to query the trained MOGP and propagate to the CAFE model, the length for both the predicted and actual values will be taken to be the melt pool length obtained by an FE model using the test case process parameters. This means that for case 1 predicted and actual, the melt pool length is assumed to be 375 μm. Likewise for case 2, the length will be 745 μm.

With predicted and actual melt pool dimensions known (Table 5), CAFE model microstructure RVEs are generated for comparison with MOGP predictions. For each of the 4 produced CAFE microstructures

Table 5
Melt pool dimension predictions and error for two test cases.

Test case #	Actual (μm)		Predicted (μm)		Error (%)	
	Width	Depth	Width	Depth	Width	Depth
1	320	84	307	76	4.06	9.52
2	176	64	186	58	5.68	9.38

Table 6
KL divergence between the MOGP predicted and actual CAFE microstructure feature distributions for both tests cases using the experimentally (EXP) derived melt pool dimensions and the MFGP derived melt pool dimensions.

Test Case #	1		2	
Melt pool	EXP	MFGP	EXP	MFGP
V	2.46	2.36	3.84	4.11
g	0.67	0.7	0.75	0.75
γ	6.02	6.68	9.08	8.97
h	2.61	2.6	1.93	1.96
r_1	1.29	1.41	3.431	3.801
r_2	0.23	0.26	0.561	0.561
r_3	0.3	0.31	0.5	0.55
phi	0.48	0.48	0.46	0.45
theta	0.25	0.25	0.29	0.26
psi	0.39	0.39	0.37	0.43

from the 2 input process parameters, the MOGP predicted and actual probability density functions can be compared using the KL divergence as was done in Section 3.2. The KL divergence values are shown in Table 6. For case 1, both the experimentally derived and MFGP derived melt pool dimensions result in divergence values that are in the range of what was seen during cross-validation (Fig. 7). For case 2, the divergence between the actual and predicted feature distributions was either on the high end of the interquartile range or outside of the range seen for the cross-validation data. This indicates that the prediction of the principal components for this case is not as good as expected (based on cross-validation results) and may have a strong effect on the accuracy of the predicted properties in the SP linkage.

With predicted melt pool dimensions and microstructure features, the SP surrogate can be queried to predict properties for both test cases as shown in Fig. 10 with four combinations of predictions as well as the real properties. In both cases, the real property is the EXP-CAFE-CPFE. What can first be noticed is that, as stated before, the fGP alone tends to over predict the stress while the models with MOGP predicted microstructure features tend to underestimate the stress. Strain does not appear to follow this same behavior. The effect of the MFGP predicted melt pool versus the actual melt pool appears to be small and shows no consistent over or under prediction affect on the mechanical properties.

While a demonstration of multiple combinations of predicted and actual components of the linkage is useful for understanding possible

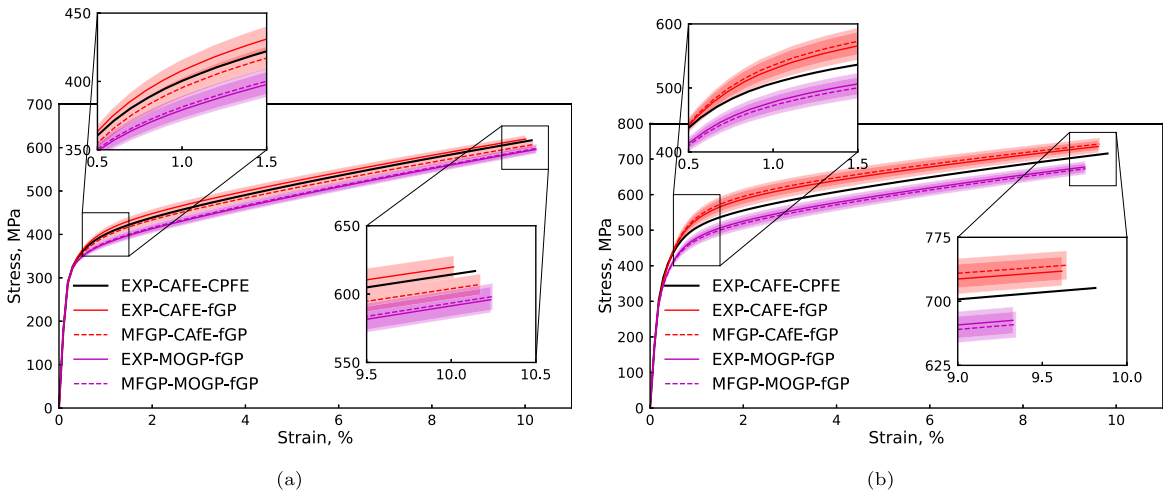

Fig. 10. fGP network predictions with 95% confidence interval for both test cases of unseen process parameters: (a) test case 1 predictions, (b) test case 2 predictions. Each figure includes the traditional experimental/simulation approach (EXP-CAFE-CPFE) along with possible combinations of surrogates and experiments/simulations.

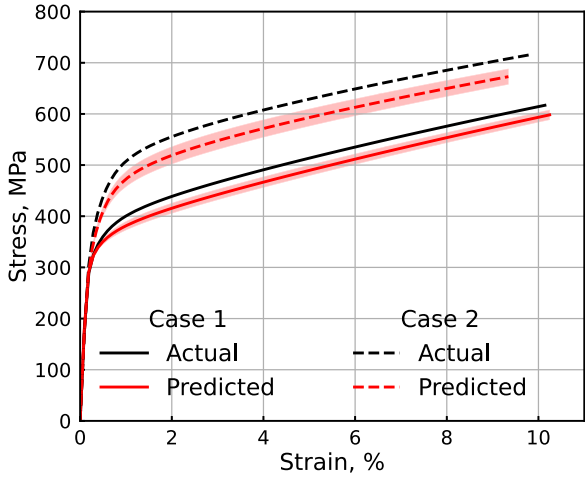

Fig. 11. PSP linkage mechanical property predictions for the actual physics-based approach and the predicted ML approach with 95% confidence interval.

Table 7
MAPE for PSP linkage mechanical property predictions for the actual physics-based approach and the predicted ML approach. Error is quantified at approximately the yield point, the final increment, and as an average over the whole prediction.

MAPE (%)	Test case 1		Test case 2	
	Strain	Stress	Strain	Stress
≈1% Strain (Yield)	1.57	4.60	9.26	8.35
Final increment	1.02	3.03	4.78	5.98
Overall	1.54	3.97	6.65	6.90

areas of improved in the PSP linkage, the most important results of Fig. 10 are the comparisons between EXP-CAFE-CPFE and MFGP-MOGP-fGP. This represents the comparison between a physics-based PSP linkage and the ML-based PSP linkage developed in this work. This comparison is shown in Fig. 11 and Table 7 for both case 1 and case 2. The primary comparison to be made here, again, is that the physics-based linkage requires multiple days of experimental and computational time whereas the ML model, once trained, requires only a few minutes of resources on standard laptop. The cost of this resource reduction is an error penalty of around 5% and <10% at the single worst point for an orders of magnitude speedup.

5. Discussion

Thus far, a novel GP-based PSP framework for L-PBF 316L stainless steel at the microscale has been demonstrated. Three surrogate models have been developed for the purpose of linking process to structure to property. In the process modeling surrogate, an MFGP was trained to multiple data sources to produce melt pool dimension predictions. While the MFGP has the flexibility to predict various quantities of interest (*e.g.*, peak temperature, solidification gradient/rate, *etc.*), melt pool dimensions are important quantities that are comparable between experiments and simulations and attainable via experiments without significant cost. By incorporating experimental data along with a range of computational models to predict melt pool geometry, the MFGP surrogate can overcome some of the challenges encountered with computational models, which include either a compromise on accuracy for analytical/low-cost models or costly simulation times for computational fluid dynamic models. Note that the CAFE model used in this work only requires melt pool geometry as a function of time, along with material properties, to drive solidification. However, in general, more features including the full thermal field history may be sought after. One possible method for incorporating other quantities of interest into the MFGP surrogate that are experimentally unobservable or difficult to obtain (including melt pool length) is to substitute experimental data with high fidelity multiphysics simulations [70]. Further, an interesting extension of the MFGP is to incorporate a functional component analogous to that in the structure–property surrogate model in order to include spatial and temporal dependence. With this structure, the process surrogate model would be capable of learning from computational simulation data to predict the full field temperature field history given a set of input build conditions.

For the process-structure surrogate, an MOGP was trained and cross-validated to relate melt pool dimensions to microstructure feature statistics. The microstructure features were reduced from 10 distributions of data for each microstructure to 20 mean and variance parameters and then to 4 principal components for each microstructure. As with the process surrogate, it is noted here that the 10 features chosen were selected to maintain continuity with the structure–property surrogate. However, the process established can be applied to other features of interest (*e.g.*, pole figure information, Schmid factor, *etc.*). Cross-validation results on the principal components was overall good

when comparing predicted values to actual values. This was reinforced by comparing predicted and actual microstructure feature distributions using the Kullback–Leibler divergence, which demonstrated that cross-validation results were almost indistinguishable from predictions on training data from the trained model (*i.e.*, deterministic predictions). One principal component was not predicted well. This is likely a result of the inputs not adequately describing that PC. While this affects the prediction accuracy, it is a relatively minor effect since that PC only explained 1% of the total variance. A possible way to address this is to add more inputs (*e.g.*, two-point statistics, more melt pool dimension descriptors, *etc.*) to the MOGP that can more completely describe all the PCs. Once the MOGP was trained and cross-validated, a test case was propagated through the MOGP. Qualitatively, the test case showed very good agreement between the predicted and actual microstructure feature distributions. Quantitatively, Kullback–Leibler divergence values were consistent with results seen when predicting training data with the trained model.

It was observed in Section 3.2, that KL divergence values for some microstructure features were relatively high and far from the ideal value of 0. This was determined to be the result of the data compression technique that transformed the distributions of the microstructural features into normal distributions. Transforming the marginal distributions of jointly distributed random variables to normal marginal distributions modifies the variables' correlation structure. This introduces errors when inverting this transformation from the joint distribution with normal marginal distributions to the target joint distribution. Alternative data compression techniques could potentially alleviate this issue. However, the cost to make these improvements may not be necessary, depending on the application. The reason the MOGP prediction errors do not lead to large errors in property prediction is that the properties (*i.e.*, stress–strain curves) are homogenized (*i.e.*, spatially averaged) quantities. Note that many traditional models link mean features (*e.g.*, mean grain size) to material properties (*e.g.*, yield strength), whereas the approach in this work considers the full distributions of 10 microstructural features, not just their mean values. Thus, errors in representing these features are offset by the large amount of information included in the analysis.

In regards to mechanical properties, a structure–property surrogate based on an fGP from a previous work was retrained using CAFE model microstructures generated for the process-structure surrogate training process. The retraining was evaluated using a withheld data set that contained 30% of the training data as well as a CAFE model microstructure that was generated using a different scan pattern than the training data. The results on the withheld data set showed average predictive accuracy over the whole stress–strain curve of <1% for strain and <3% for stress. Similarly, predictions on the unseen CAFE microstructure demonstrated <4% error for both stress and strain. Interestingly, this was the case even though the scan pattern was different for the unseen microstructure and the microstructures used for training. The fGP is trained in such a way that it only learns grain features and is demonstrating an agnosticism to the scan pattern and, more generally, the process parameters. By having a structure–property surrogate that is agnostic to the process parameters, then training of the surrogate can be completed on any representative data set that exhibits the necessary range of grain features. If this were not the case, then the structure–property surrogate training would depend on unique microstructures from the process-structure surrogate and make training both surrogates sequential and inefficient. Whereas the methodology applied here for the structure–property surrogate means that training of the SP and PS surrogates can be accomplished in parallel.

One feature that was noted in predictions from the fGP was that they tended to overpredicted the stress when microstructure features derived directly from a CAFE model were used. Conversely, when the MOGP data was used as the input to the fGP, an under-prediction was consistently seen. The overprediction is simply a result of how the model was trained and is demonstrated by the prediction on the withheld data (Fig. 8(a)). The under-prediction from the MOGP has to do with learned features from the microstructure and how the constitutive model handles these features. The underlying constitutive model is affected by grain size and shape such that very small or very elongated grains have a strain hardened effect (*i.e.*, an increase in apparent yield strength with a corresponding decrease in hardening modulus). Due to the way that the quantile and normal transformations are done in the MOGP, the predictions tend to be more concentrated at the central portion of the distribution. In the central portion of the distribution, the predicted grain parameters tend to be less elongated and of a more moderate size resulting in a lower prediction of mechanical properties. This phenomenon, as mentioned, is a result of the choice of constitutive model that was used to train the fGP. However, the fGP is designed and implemented in such a way that it can be trained on any crystal plasticity model that relates grain features to mechanical properties. Thus, as new models are developed (*e.g.*, [71]), the fGP could be retrained to emulate the newer, more advanced constitutive model.

In both cases of over or under prediction, one issue of note with the predictions, particularly in Fig. 11, are that the actual solutions do not fall within the confidence interval (CI) from the fGP. This is a result of the CI only being the predicted standard deviation from the fGP model trained on stress as a function of displacement. In order to get a complete CI, uncertainty propagation from the beginning process parameters is necessary, which would account for uncertainty in the MFGP, MOGP, and both fGPs used in the SP surrogate. While doing this is beyond the scope of this work, other works have already demonstrated the feasibility of linking multiple GPs in AM then quantifying and propagating uncertainty using Bayesian approaches [72]. Doing so would increase the CIs of the predicted values and, given the small difference between the actual and predicted values, would likely result in the actual value being encompassed by the CI of the predicted value.

It is inevitable that model form error exists for fast-running ML-based surrogate models for PSP linkages. The primary approach to reduce prediction error is to generate more training data. In practice, there must be a balance made among data collection costs, training time, and accuracy. Data set size is limited when high fidelity simulations or experiments are required. The training time associated with optimizing the parameters of surrogate models also increases with the size of training data sets. For example, the training time of GPs scales as $\mathcal{O}(n^3)$ for n being the number of data points. Ultimately the size of the data set depends on the acceptable error tolerance balanced with the cost of obtaining data, which is application-specific.

While the framework has been developed and trained using a single AM process and material, there is no inherent restriction in the framework that limits it to a single material or process. In fact, each of the GP models is quite flexible and could be modified to account for additional material or constitutive parameters as part of the input parameter space. An interesting concept for materials design could be to train the GPs in such a way that material composition and process parameters are input and, from these compositions, material parameters for the thermal, microstructure, and mechanical models could be obtained (possibly through another ML model). Doing so would allow materials scientists to study desired compositions that result in certain properties and drastically reduce the search space for new candidate AM materials.

6. Summary

A GP-based PSP relation linkage for L-PBF 316L stainless steel at the microscale has been developed and demonstrated. This linkage first relates the process parameters to melt pool dimensions, then links these to microstructure feature statistics, and ultimately to mechanical properties through a series of 3 GP surrogates. Each of the surrogates is trained on a limited set of data and demonstrated high predictive accuracy through validation either using a test set method or cross-validation method. The linked GPs were shown to be accurate on

two previously unseen sets of process parameters, yielding around 95% accuracy in the mechanical property predictions with an orders of magnitude reduction in prediction time compared to traditional experimental or simulation approaches. Each surrogate has room for improvement, such as refinements to the MOGP through incorporation of spatial statistics or additional descriptors and improvements to the dimensionality reduction process. However, to better focus improvement efforts, a Bayesian analysis on the full linkage is needed to determine which surrogate model results in the largest sources of error. Performing this Bayesian analysis will demonstrate the feasibility of sampling the linkage 100 s or 1000 s of times and allow more thorough uncertainty propagation or quantification work to assess how changes in process parameters manifest as changes in microstructure features and mechanical properties. Furthermore, the Bayesian treatment of this first of its kind surrogate linkage will enable inverse PSP relationship determination where desired mechanical properties are input and a range of process parameters producing these properties can be obtained including uncertainty estimates.

CRediT authorship contribution statement

Robert N. Saunders: Writing – review & editing, Writing – original draft, Visualization, Validation, Software, Methodology, Investigation, Formal analysis, Data curation, Conceptualization. **Kirubel Teferra:** Writing – review & editing, Supervision, Software. **Alaa Elwany:** Writing – review & editing, Supervision, Project administration, Conceptualization. **John G. Michopoulos:** Writing – review & editing, Supervision, Resources, Funding acquisition. **Dimitris Lagoudas:** Writing – review & editing, Supervision, Resources, Methodology.

Declaration of competing interest

The authors declare that they have no known competing financial interests or personal relationships that could have appeared to influence the work reported in this paper.

Data availability

The raw/processed data required to reproduce these findings cannot be shared at this time as the data also forms part of an ongoing study.

Acknowledgments

RS, KT, and JM acknowledge partial support for this work by the Office of Naval Research through the Naval Research Laboratory's (NRL), United States core funding. RS acknowledges partial support for this work by the NRL Edison Graduate Memorial Training Program. This work was supported in part by a grant of computer time from the DOD High Performance Computing Modernization Program at the Air Force Research Laboratory (AFRL) DoD Supercomputing Resource Centers (DSRC).

Appendix. Gaussian process modeling

In the following derivation, standard GP regression theory is briefly overviewed but for complete details, the interested reader is directed to the landmark work of Rasmussen and Williams [73]. First, let $\boldsymbol{X} = (\boldsymbol{x}_1, \dots, \boldsymbol{x}_n)^T$ denote the vector of input vector variables, $Y = (y_1, \dots, y_n)^T$ denote corresponding scalar outputs, and $D = \{\boldsymbol{x}_i, y_i\} = (\boldsymbol{X}, Y)$ for $i = 1, \dots, n$ denote the joint dataset of $\boldsymbol{X}$ and Y, and let $f(\cdot)$ be an unknown stochastic process. A GP is a non-parametric statistical model in which $f(\cdot)$ follows an n-dimensional multivariate Gaussian:

$$p(f(\boldsymbol{x}_1), \dots, f(\boldsymbol{x}_n)) \sim \mathcal{N}_n(\boldsymbol{\mu}, \boldsymbol{k}), \tag{A.1}$$

where $\boldsymbol{\mu}$ is the mean vector defined by the mean function $\mu(\boldsymbol{x}_i) \equiv \boldsymbol{\mu}_i = \mathbb{E}\left[f(\boldsymbol{x}_i)\right]$ and $\boldsymbol{k}$ is the covariance defined by the covariance function $k(\boldsymbol{x}_i, \boldsymbol{x}_j) \equiv \boldsymbol{k}_{ij} = cov\left[f(\boldsymbol{x}_i), f(\boldsymbol{x}_j)\right]$. Now, the Gaussian process can be denoted as $f(\cdot) \sim \mathcal{GP}(\mu(\cdot), k(\cdot, \cdot))$. The standard problem of nonlinear regression takes the form

$$y_i(\boldsymbol{x}_i) = f(\boldsymbol{x}_i) + \epsilon_i, \tag{A.2}$$

where f is as above and follows a GP, and ϵ_i are independent and identically distributed (i.i.d) Gaussian random noise with 0 mean and σ^2 variance. It then follows that

$$Y = (y_1, \dots, y_n)^T \sim \mathcal{N}(\boldsymbol{\mu}, \boldsymbol{K}), \tag{A.3}$$

where $\boldsymbol{\mu} = (\boldsymbol{\mu}_1, \dots, \boldsymbol{\mu}_n)^T$ and $\boldsymbol{K} = \boldsymbol{k}_{ij} + \sigma^2 \boldsymbol{I}$, where $\boldsymbol{I}$ is the $n \times n$ identity matrix. The assumption of Normality is crucial to the GP framework as it allows the specification of a mean and covariance functions that define the presumed relationship between data points. Throughout this work, we will employ the common assumption that this and all other GPs are zero mean (*i.e.*, $\boldsymbol{\mu}(\cdot) = \boldsymbol{0}$). Furthermore, while the covariance function can take many forms, we will utilize either the Matérn 3/2 or squared exponential covariance; both of which are standard in GP modeling. Estimation of the parameters of the covariance functions can be obtained through frequentist or Bayesian approaches. The current work will utilize maximum likelihood estimate (MLE).

A.1. Multifidelity GP

The MFGP is a GP that is capable of fusing information from various fidelity information sources [74–76]. MFGP modeling limits the number of expensive simulations and/or experiments needed to build a model by leveraging information from inexpensive low fidelity solutions to the same problem. As such, in the context of multifidelity modeling, there are now multiple data sets from each fidelity such that $\mathcal{D}_t = (\boldsymbol{X}_t, Y_t)$ for $t = 1, \dots, s$ with the s-level being the highest fidelity, the first level being the lowest, and each level t containing n_t samples. Note that $\boldsymbol{X}_t = (\boldsymbol{x}_{t,1}, \dots, \boldsymbol{x}_{t,n_t})^T$ and $Y_t = (y_{t,1}, \dots, y_{t,n_t})^T$ still hold as above with the addition of an extra subscript for the fidelity. However, for simplicity, the sample subscript (*i.e.*, $1, \dots, n_t$) is omitted. The most popular variant of the MFGP is the one developed by Kennedy and O'Hagan [74], commonly referred to as the Kennedy–O'Hagan or KOH model. In this model, the s levels are recursively correlated as

$$f_t(\boldsymbol{x}) = \rho f_{t-1}(\boldsymbol{x}) + \delta_t(\boldsymbol{x}), \tag{A.4}$$

where ρ is a scaling factor that linearly correlates the t and $t-1$ fidelities and the bias of the lower fidelity is captured by another zero mean GP as $\delta_t(\boldsymbol{x}) \sim \mathcal{GP}(0, k_t(\cdot, \cdot))$. There are two primary drawbacks to this implementation. First, it is numerically inefficient due to a matrix inversion containing the data from all data sets combined and, second, the form in Eq. (A.4) assumes a linear correlation between the fidelities. Recent work by Le Gratiet et al. [48,49] has addressed the issue of inefficiency while Perdikaris et al. [77] have addressed the linear correlation limitation.

The KOH model was made more efficient in Le Gratiet et al. by replacing the GP prior $f_{t-1}(\boldsymbol{x})$ with the corresponding posterior $f^*_{t-1}(\boldsymbol{x})$ while enforcing $\mathcal{D}_t \subseteq \mathcal{D}_{t-1}$. Since nested data is enforced (*i.e.*, data from fidelity t is a subset of the points in fidelity $t-1$), the posterior predictive distribution $f^*_{t-1}(\boldsymbol{x})$ is deterministic at $\boldsymbol{x}$, which essentially decouples the MFGP problem into s standard GP problems.

To account for non-linear correlations, Perdikaris et al. modified Eq. (A.4) as

$$f_t(\boldsymbol{x}) = z_{t-1}(f_{t-1}(\boldsymbol{x})) + \delta_t(\boldsymbol{x}), \tag{A.5}$$

where $z_{t-1}(\cdot)$ is an unknown function that maps the lower fidelity to the higher fidelity and is assigned a GP prior. By assigning a GP prior to $z_{t-1}(\cdot)$, the posterior of $f_t(\cdot)$ is no longer Gaussian, but this nested GP structure can be made more tractable by following the scheme of Le Gratiet et al. and replacing the prior of fidelity $t-1$ with the posterior as

$$f_t(\boldsymbol{x}) = z_{t-1}(f^*_{t-1}(\boldsymbol{x})) + \delta_t(\boldsymbol{x}) = g_t(\boldsymbol{x}, f^*_{t-1}(\boldsymbol{x})), \tag{A.6}$$

where $g_t(\boldsymbol{x})$ leverages the independence of $z_{t-1}(f^*_{t-1}(\boldsymbol{x}))$ and $\delta_t(\boldsymbol{x})$ and the fact that the sum of two GPs results in another GP. In this work, the covariance function of g_t takes the decomposed form of

$$k_{t_g} = k_{t_\rho}(\boldsymbol{x}, \boldsymbol{x}') \cdot k_{t_f}(f^*_{t-1}(\boldsymbol{x}), f^*_{t-1}(\boldsymbol{x}')) + k_{t_\delta}(\boldsymbol{x}, \boldsymbol{x}'), \tag{A.7}$$

where each k_t is a valid covariance function. The MFGP will implement the squared exponential covariance for each kernel k_{t_ρ}, k_{t_f}, and k_{t_δ}, which results in a nonlinear correlation between $f_t(\cdot)$ and $f_{t-1}(\cdot)$. In particular, when k_{t_δ} takes the form as specified, it will result in a nonlinear correlation, but in portions of this work, a linear correlation will be used to evaluate the efficacy of a linear versus nonlinear correlation. This will result in $k_{t_\delta}(\boldsymbol{x}, \boldsymbol{x}')$ taking the form of a bias or constant kernel.

A.2. Multioutput GP

The MOGP is a modification of the standard GP that accounts for multiple, coupled, outputs such that $\boldsymbol{Y} = (\boldsymbol{y}_1, \ldots, \boldsymbol{y}_n)^T$ is now also a vector with dimensions $q \times n$. To account for this modification, Eq. (A.3) is modified to consider correlation between the outputs as follows:

$$\boldsymbol{Y} = (\boldsymbol{y}_1, \ldots, \boldsymbol{y}_n)^T \sim \mathcal{N}_q(\boldsymbol{\mu}, \boldsymbol{K}\boldsymbol{\Sigma}), \tag{A.8}$$

where $\boldsymbol{\Sigma}$ is a $q \times q$ correlation matrix between the outputs. The matrix $\boldsymbol{\Sigma}$ can consider correlation between each output and every other output if it is fully populated [76,78]. In this work, however, the elements of each $\boldsymbol{y}_i$ are treated as independent such that $\boldsymbol{\Sigma} = \boldsymbol{I}$. This is motivated by the choice of outputs and their independence from each other that will be discussed in Section 2.2.

A.3. Functional GP

In the above formulations, each $\boldsymbol{x}_i$ takes the form of a vector with scalar components while each y_i is a scalar or a vector of scalars. However, it is possible for each $\boldsymbol{x}_i$ and y_i to be functions of another variable, such as time. When this is the case, functional data analysis (FDA) can be combined with GP modeling to construct a functional GP (fGP) [79]. For brevity, the full details of the fGP are omitted and can be found in [68,79]. A brief overview is provided here. The fGP modifies Eq. (A.2) to be of the form

$$Y_i(t) = f(\boldsymbol{X}_i(t), \boldsymbol{z}_i) + \epsilon_i(t), \ t \in \mathcal{T}, \tag{A.9}$$

where $Y_i(\cdot)$ are now the 1-dimensional functional parameters, $\boldsymbol{X}_i(\cdot)$ are the q-dimensional functional parameters, $\boldsymbol{z}_i$ now represent p-dimensional scalar parameters, and the Gaussian noise is now functional as well with mean zero and variance σ^2_ϵ. This problem, however, is not well defined since functional data resides in an infinite dimensional space. This can be resolved by utilizing functional principal component analysis (fPCA) and decomposing $Y_i(t)$ into a functional mean, functional principal components, and covariance eigenfunctions. The functional mean, eigenfunctions, and the noise variance do not depend on the sample i and as such can be determined using FDA methods without the use of a GP. This reduces the problem of determining $Y_i(t)$ to an application of FDA methods that act as a linear shift and scaling of the data such that it has a zero mean, and the fitting of an fGP that relates input parameters to each functional principal component. The covariance for each of the fGPs will take the form of a Matérn 3/2.

References

[1] D. Herzog, V. Seyda, E. Wycisk, C. Emmelmann, Additive manufacturing of metals, Acta Mater. 117 (2016) 371–392, http://dx.doi.org/10.1016/j.actamat.2016.07.019, URL http://dx.doi.org/10.1016/j.actamat.2016.07.019https://linkinghub.elsevier.com/retrieve/pii/S1359645416305158.

[2] Y.M. Wang, T. Voisin, J.T. McKeown, J. Ye, N.P. Calta, Z. Li, Z. Zeng, Y. Zhang, W. Chen, T.T. Roehling, R.T. Ott, M.K. Santala, P.J. Depond, M.J. Matthews, A.V. Hamza, T. Zhu, Additively manufactured hierarchical stainless steels with high strength and ductility, Nature Mater. 17 (1) (2018) 63–71, http://dx.doi.org/10.1038/nmat5021, URL http://www.nature.com/doifinder/10.1038/nmat5021http://www.nature.com/articles/nmat5021.

[3] N.C. Ferreri, R. Pokharel, V. Livescu, D.W. Brown, M. Knezevic, J.S. Park, M.A. Torrez, G.T. Gray, Effects of heat treatment and build orientation on the evolution of ϵ and $\alpha\prime$ martensite and strength during compressive loading of additively manufactured 304L stainless steel, Acta Mater. 195 (2020) 59–70, http://dx.doi.org/10.1016/j.actamat.2020.04.036.

[4] A. Molkeri, D. Khatamsaz, R. Couperthwaite, J. James, R. Arróyave, D. Allaire, A. Srivastava, On the importance of microstructure information in materials design: PSP vs PP, Acta Mater. 223 (2022) 117471, http://dx.doi.org/10.1016/j.actamat.2021.117471.

[5] D. Gunasegaram, A. Murphy, A. Barnard, T. DebRoy, M. Matthews, L. Ladani, D. Gu, Towards developing multiscale-multiphysics models and their surrogates for digital twins of metal additive manufacturing, Addit. Manuf. 46 (February) (2021) 102089, http://dx.doi.org/10.1016/j.addma.2021.102089, URL https://linkinghub.elsevier.com/retrieve/pii/S2214860421002542.

[6] J.H. Panchal, S.R. Kalidindi, D.L. McDowell, Key computational modeling issues in Integrated Computational Materials Engineering, Comput. Aided Des. 45 (1) (2013) 4–25, http://dx.doi.org/10.1016/j.cad.2012.06.006, URL http://dx.doi.org/10.1016/j.cad.2012.06.006https://linkinghub.elsevier.com/retrieve/pii/S0010448512001352.

[7] J. Smith, W. Xiong, W. Yan, S. Lin, P. Cheng, O.L. Kafka, G.J. Wagner, J. Cao, W.K. Liu, Linking process, structure, property, and performance for metal-based additive manufacturing: computational approaches with experimental support, Comput. Mech. 57 (4) (2016) 583–610, http://dx.doi.org/10.1007/s00466-015-1240-4, URL http://link.springer.com/10.1007/s00466-015-1240-4.

[8] M. Francois, A. Sun, W. King, N. Henson, D. Tourret, C. Bronkhorst, N. Carlson, C. Newman, T. Haut, J. Bakosi, J. Gibbs, V. Livescu, S. Vander Wiel, A. Clarke, M. Schraad, T. Blacker, H. Lim, T. Rodgers, S. Owen, F. Abdeljawad, J. Madison, A. Anderson, J.-L. Fattebert, R. Ferencz, N. Hodge, S. Khairallah, O. Walton, Modeling of additive manufacturing processes for metals: Challenges and opportunities, Curr. Opin. Solid State Mater. Sci. 21 (4) (2017) 198–206, http://dx.doi.org/10.1016/j.cossms.2016.12.001, URL http://dx.doi.org/10.1016/j.cossms.2016.12.001https://linkinghub.elsevier.com/retrieve/pii/S1359028616300833, arXiv:1709.09510.

[9] M. Markl, C. Körner, Multiscale modeling of powder bed–based additive manufacturing, Annu. Rev. Mater. Res. 46 (1) (2016) 93–123, http://dx.doi.org/10.1146/annurev-matsci-070115-032158, arXiv:1406.3533, URL http://www.annualreviews.org/doi/10.1146/annurev-matsci-070115-032158.

[10] H. Lim, F. Abdeljawad, S.J. Owen, B.W. Hanks, J.W. Foulk, C.C. Battaile, Incorporating physically-based microstructures in materials modeling: Bridging phase field and crystal plasticity frameworks, Modelling Simul. Mater. Sci. Eng. 24 (4) (2016) 045016, http://dx.doi.org/10.1088/0965-0393/24/4/045016, URL https://iopscience.iop.org/article/10.1088/0965-0393/24/4/045016.

[11] M. Diehl, M. Groeber, C. Haase, D.A. Molodov, F. Roters, D. Raabe, Identifying structure–property relationships through dream.3D representative volume elements and DAMASK crystal plasticity simulations: An integrated computational materials engineering approach, JOM 69 (5) (2017) 848–855, http://dx.doi.org/10.1007/s11837-017-2303-0, URL http://link.springer.com/10.1007/s11837-017-2303-0.

[12] S. Mahadevan, P. Nath, Z. Hu, Uncertainty quantification for additive manufacturing process improvement: Recent advances, ASCE-ASME J. Risk Uncert Eng. Syst. B Mech. Eng. 8 (1) (2022) http://dx.doi.org/10.1115/1.4053184, URL https://asmedigitalcollection.asme.org/risk/article/8/1/010801/1129174/Uncertainty-Quantification-for-Additive.

[13] T. Mukherjee, T. DebRoy, A digital twin for rapid qualification of 3D printed metallic components, Appl. Mater. Today 14 (2019) 59–65, http://dx.doi.org/10.1016/j.apmt.2018.11.003, URL https://doi.org/10.1016/j.apmt.2018.11.003https://linkinghub.elsevier.com/retrieve/pii/S2352940718304931.

[14] S.R. Kalidindi, M. De Graef, Materials data science: Current status and future outlook, Annu. Rev. Mater. Res. 45 (1) (2015) 171–193, http://dx.doi.org/10.1146/annurev-matsci-070214-020844, URL http://www.annualreviews.org/doi/10.1146/annurev-matsci-070214-020844.

[15] A. Agrawal, A. Choudhary, Perspective: Materials informatics and big data: Realization of the "fourth paradigm" of science in materials science, APL Mater. 4 (5) (2016) 053208, http://dx.doi.org/10.1063/1.4946894, URL http://aip.scitation.org/doi/10.1063/1.4946894.

[16] D.M. Dimiduk, E.A. Holm, S.R. Niezgoda, Perspectives on the impact of machine learning, deep learning, and artificial intelligence on materials, processes, and structures engineering, Integr Mater Manuf Innov 7 (3) (2018) 157–172, http://dx.doi.org/10.1007/s40192-018-0117-8, URL http://link.springer.com/10.1007/s40192-018-0117-8.

[17] F.E. Bock, R.C. Aydin, C.J. Cyron, N. Huber, S.R. Kalidindi, B. Klusemann, A review of the application of machine learning and data mining approaches in continuum materials mechanics, Front. Mater. 6 (May) (2019) http://dx.doi.org/10.3389/fmats.2019.00110, URL https://www.frontiersin.org/article/10.3389/fmats.2019.00110/full.

[18] T. Lookman, P.V. Balachandran, D. Xue, R. Yuan, Active learning in materials science with emphasis on adaptive sampling using uncertainties for targeted design, Npj Comput Mater 5 (1) (2019) 21, http://dx.doi.org/10.1038/s41524-019-0153-8, URL http://www.nature.com/articles/s41524-019-0153-8.

[19] D.L. McDowell, R.A. LeSar, The need for microstructure informatics in process–structure–property relations, MRS Bull. 41 (08) (2016) 587–593, http://dx.doi.org/10.1557/mrs.2016.163, URL http://link.springer.com/10.1557/mrs.2016.163.

[20] S.R. Kalidindi, A.J. Medford, D.L. McDowell, Vision for data and informatics in the future materials innovation ecosystem, JOM 68 (8) (2016) 2126–2137, http://dx.doi.org/10.1007/s11837-016-2036-5, URL http://link.springer.com/10.1007/s11837-016-2036-5.

[21] R. Ramprasad, R. Batra, G. Pilania, A. Mannodi-Kanakkithodi, C. Kim, Machine learning in materials informatics: recent applications and prospects, Npj Comput Mater 3 (1) (2017) 54, http://dx.doi.org/10.1038/s41524-017-0056-5, arXiv:1707.07294, URL http://dx.doi.org/10.1038/s41524-017-0056-5http://www.nature.com/articles/s41524-017-0056-5.

[22] S. Ramakrishna, T.-Y. Zhang, W.-C. Lu, Q. Qian, J.S.C. Low, J.H.R. Yune, D.Z.L. Tan, S. Bressan, S. Sanvito, S.R. Kalidindi, Materials informatics, J. Intell. Manuf. 30 (6) (2019) 2307–2326, http://dx.doi.org/10.1007/s10845-018-1392-0, URL https://doi.org/10.1007/s10845-018-1392-0http://link.springer.com/10.1007/s10845-018-1392-0.

[23] D.B. Brough, D. Wheeler, J.A. Warren, S.R. Kalidindi, Microstructure-based knowledge systems for capturing process-structure evolution linkages, Curr. Opin. Solid State Mater. Sci. 21 (3) (2017) 129–140, http://dx.doi.org/10.1016/j.cossms.2016.05.002, URL http://dx.doi.org/10.1016/j.cossms.2016.05.002https://linkinghub.elsevier.com/retrieve/pii/S1359028616300298.

[24] R. Liu, A. Kumar, Z. Chen, A. Agrawal, V. Sundararaghavan, A. Choudhary, A predictive machine learning approach for microstructure optimization and materials design, Sci. Rep. 5 (1) (2015) 11551, http://dx.doi.org/10.1038/srep11551, URL http://www.nature.com/articles/srep11551.

[25] N.H. Paulson, M.W. Priddy, D.L. McDowell, S.R. Kalidindi, Reduced-order structure-property linkages for polycrystalline microstructures based on 2-point statistics, Acta Mater. 129 (2017) 428–438, http://dx.doi.org/10.1016/j.actamat.2017.03.009, URL http://dx.doi.org/10.1016/j.actamat.2017.03.009https://linkinghub.elsevier.com/retrieve/pii/S135964541730188X.

[26] Z. Yang, Y.C. Yabansu, R. Al-Bahrani, W.-k. Liao, A.N. Choudhary, S.R. Kalidindi, A. Agrawal, Deep learning approaches for mining structure-property linkages in high contrast composites from simulation datasets, Comput. Mater. Sci. 151 (April) (2018) 278–287, http://dx.doi.org/10.1016/j.commatsci.2018.05.014, URL https://linkinghub.elsevier.com/retrieve/pii/S0927025618303215.

[27] A. Khosravani, A. Cecen, S.R. Kalidindi, Development of high throughput assays for establishing process-structure-property linkages in multiphase polycrystalline metals: Application to dual-phase steels, Acta Mater. 123 (2017) 55–69, http://dx.doi.org/10.1016/j.actamat.2016.10.033, URL http://dx.doi.org/10.1016/j.actamat.2016.10.033https://linkinghub.elsevier.com/retrieve/pii/S135964541630800X.

[28] X. Qi, G. Chen, Y. Li, X. Cheng, C. Li, Applying neural-network-based machine learning to additive manufacturing: Current applications, challenges, and future perspectives, Engineering 5 (4) (2019) 721–729, http://dx.doi.org/10.1016/j.eng.2019.04.012.

[29] C. Wang, X.P. Tan, S.B. Tor, C.S. Lim, Machine learning in additive manufacturing: State-of-the-art and perspectives, Addit. Manuf. 36 (January) (2020) 101538, http://dx.doi.org/10.1016/j.addma.2020.101538.

[30] N.S. Johnson, P.S. Vulimiri, A.C. To, X. Zhang, C.A. Brice, B.B. Kappes, A.P. Stebner, Invited review: Machine learning for materials developments in metals additive manufacturing, Addit. Manuf. 36 (2020) http://dx.doi.org/10.1016/j.addma.2020.101641.

[31] L. Jannesari Ladani, Applications of artificial intelligence and machine learning in metal additive manufacturing, J. Phys.: Mater. 4 (4) (2021) 042009, http://dx.doi.org/10.1088/2515-7639/ac2791, URL https://iopscience.iop.org/article/10.1088/2515-7639/ac2791.

[32] J. Qin, F. Hu, Y. Liu, P. Witherell, C.C. Wang, D.W. Rosen, T.W. Simpson, Y. Lu, Q. Tang, Research and application of machine learning for additive manufacturing, Addit. Manuf. 52 (February) (2022) http://dx.doi.org/10.1016/j.addma.2022.102691.

[33] W. Yan, Y. Lian, C. Yu, O.L. Kafka, Z. Liu, W.K. Liu, G.J. Wagner, An integrated process–structure–property modeling framework for additive manufacturing, Comput. Methods Appl. Mech. Engrg. 339 (2018) 184–204, http://dx.doi.org/10.1016/j.cma.2018.05.004, URL https://doi.org/10.1016/j.cma.2018.05.004https://linkinghub.elsevier.com/retrieve/pii/S0045782518302391.

[34] W. Yan, S. Lin, O.L. Kafka, Y. Lian, C. Yu, Z. Liu, J. Yan, S. Wolff, H. Wu, E. Ndip-Agbor, M. Mozaffar, K. Ehmann, J. Cao, G.J. Wagner, W.K. Liu, Data-driven multi-scale multi-physics models to derive process–structure–property relationships for additive manufacturing, Comput. Mech. 61 (5) (2018) 521–541, http://dx.doi.org/10.1007/s00466-018-1539-z, URL https://doi.org/10.1007/s00466-018-1539-zhttp://link.springer.com/10.1007/s00466-018-1539-z.

[35] P. Liu, Z. Wang, Y. Xiao, R. Lebensohn, Y. Liu, M. Horstemeyer, X. Cui, L. Chen, Integration of phase-field model and crystal plasticity for the prediction of process-structure-property relation of additively manufactured metallic materials, Int. J. Plast. 128 (January) (2020) 102670, http://dx.doi.org/10.1016/j.ijplas.2020.102670, URL https://doi.org/10.1016/j.ijplas.2020.102670https://linkinghub.elsevier.com/retrieve/pii/S0749641919305017.

[36] J.A. Turner, J. Belak, N. Barton, M. Bement, N. Carlson, R. Carson, S. DeWitt, J.L. Fattebert, N. Hodge, Z. Jibben, W. King, L. Levine, C. Newman, A. Plotkowski, B. Radhakrishnan, S.T. Reeve, M. Rolchigo, A. Sabau, S. Slattery, B. Stump, ExaAM: Metal additive manufacturing simulation at the fidelity of the microstructure, Int. J. High Perform. Comput. Appl. 36 (1) (2022) 13–39, http://dx.doi.org/10.1177/10943420211042558.

[37] T. DebRoy, H. Wei, J. Zuback, T. Mukherjee, J. Elmer, J. Milewski, A. Beese, A. Wilson-Heid, A. De, W. Zhang, Additive manufacturing of metallic components – Process, structure and properties, Prog. Mater. Sci. 92 (2018) 112–224, http://dx.doi.org/10.1016/j.pmatsci.2017.10.001, URL https://linkinghub.elsevier.com/retrieve/pii/S0079642517301172.

[38] N. Kouraytem, X. Li, W. Tan, B. Kappes, A.D. Spear, Modeling process–structure–property relationships in metal additive manufacturing: a review on physics-driven versus data-driven approaches, J. Phys.: Mater. 4 (3) (2021) 032002, http://dx.doi.org/10.1088/2515-7639/abca7b, URL https://iopscience.iop.org/article/10.1088/2515-7639/abca7b.

[39] Z. Wang, W. Yang, Q. Liu, Y. Zhao, P. Liu, D. Wu, M. Banu, L. Chen, Data-driven modeling of process, structure and property in additive manufacturing: A review and future directions, J. Manuf. Process. 77 (March) (2022) 13–31, http://dx.doi.org/10.1016/j.jmapro.2022.02.053.

[40] Z. Wang, P. Liu, Y. Ji, S. Mahadevan, M.F. Horstemeyer, Z. Hu, L. Chen, L.-Q. Chen, Uncertainty quantification in metallic additive manufacturing through physics-informed data-driven modeling, JOM 71 (8) (2019) 2625–2634, http://dx.doi.org/10.1007/s11837-019-03555-z, URL https://doi.org/10.1007/s11837-019-03555-zhttp://link.springer.com/10.1007/s11837-019-03555-z.

[41] C. Kamath, Y.J. Fan, Regression with small data sets: a case study using code surrogates in additive manufacturing, Knowl. Inf. Syst. 57 (2) (2018) 475–493, http://dx.doi.org/10.1007/s10115-018-1174-1.

[42] Z. Yan, W. Liu, Z. Tang, X. Liu, N. Zhang, M. Li, H. Zhang, Review on thermal analysis in laser-based additive manufacturing, Opt. Laser Technol. 106 (2018) 427–441, http://dx.doi.org/10.1016/j.optlastec.2018.04.034.

[43] R. Saunders, A. Rawlings, A. Birnbaum, A. Iliopoulos, J. Michopoulos, D. Lagoudas, A. Elwany, Additive manufacturing melt pool prediction and classification via multifidelity Gaussian process surrogates, Integr. Mater. Manuf. Innov. (2022) http://dx.doi.org/10.1007/s40192-022-00276-1.

[44] T. Eagar, N.-S. TSAI, Temperature Fields Produced by Traveling Distributed Heat Sources Use of a Gaussian heat distribution in dimensionless form indicates final weld pool shape can be predicted accurately for many welds and materials, Weld. J. (Miami, Fla) 62 (December) (1983).

[45] J.C. Steuben, A.J. Birnbaum, A.P. Iliopoulos, J.G. Michopoulos, Toward feedback control for additive manufacturing processes via enriched analytical solutions, J. Comput. Inf. Sci. Eng. 19 (3) (2019) http://dx.doi.org/10.1115/1.4042105.

[46] J.C. Steuben, A.J. Birnbaum, J.G. Michopoulos, A.P. Iliopoulos, Enriched analytical solutions for additive manufacturing modeling and simulation, Addit. Manuf. 25 (October 2018) (2019) 437–447, http://dx.doi.org/10.1016/j.addma.2018.10.017.

[47] A.L.K. Rawlings, A.J. Birnbaum, J.G. Michopoulos, J.C. Steuben, A.P. Iliopoulos, H. Ryou, Simulation informed effects of solidification rate on 316l single tracks produced by selective laser melting, in: Volume 9: 40th Computers and Information in Engineering Conference (CIE), (February 2021) American Society of Mechanical Engineers, 2020, http://dx.doi.org/10.1115/DETC2020-22451, URL https://asmedigitalcollection.asme.org/IDETC-CIE/proceedings/IDETC-CIE2020/83983/Virtual,Online/1090040.

[48] L. Le Gratiet, J. Garnier, Recursive co-kriging model for design of computer experiments with multiple levels of fidelity, Int. J. Uncertain. Quantif. 4 (5) (2014) 365–386, http://dx.doi.org/10.1615/Int.J.UncertaintyQuantification.2014006914, arXiv:1210.0686, URL http://arxiv.org/abs/1210.0686http://www.dl.begellhouse.com/journals/52034eb04b657aea,2f7b99cc281f2702,4c83626c5e64207a.html.

[49] L. Le Gratiet, C. Cannamela, Cokriging-based sequential design strategies using fast cross-validation techniques for multi-fidelity computer codes, Technometrics 57 (3) (2015) 418–427, http://dx.doi.org/10.1080/00401706.2014.928233, URL http://www.tandfonline.com/doi/full/10.1080/00401706.2014.928233.

[50] S.R. Kalidindi, S.R. Niezgoda, A.A. Salem, Microstructure informatics using higher-order statistics and efficient data-mining protocols, Jom 63 (4) (2011) 34–41, http://dx.doi.org/10.1007/s11837-011-0057-7.

[51] M.A. Groeber, M.A. Jackson, DREAM.3D: A digital representation environment for the analysis of microstructure in 3D, Integr. Mater. Manuf. Innov. 3 (1) (2014) 5, http://dx.doi.org/10.1186/2193-9772-3-5, URL http://link.springer.com/10.1186/2193-9772-3-5.

[52] A. Choudhury, Y.C. Yabansu, S.R. Kalidindi, A. Dennstedt, Quantification and classification of microstructures in ternary eutectic alloys using 2-point spatial correlations and principal component analyses, Acta Mater. 110 (2016) 131–141, http://dx.doi.org/10.1016/j.actamat.2016.03.010, URL http://dx.doi.org/10.1016/j.actamat.2016.03.010.

[53] E. Popova, T.M. Rodgers, X. Gong, A. Cecen, J.D. Madison, S.R. Kalidindi, Process-structure linkages using a data science approach: Application to simulated additive manufacturing data, Integr. Mater. Manuf. Innov. 6 (1) (2017) 54–68, http://dx.doi.org/10.1007/s40192-017-0088-1, URL http://link.springer.com/10.1007/s40192-017-0088-1.

[54] K. Teferra, D.J. Rowenhorst, Optimizing the cellular automata finite element model for additive manufacturing to simulate large microstructures, Acta Mater. (2021) 116930, http://dx.doi.org/10.1016/j.actamat.2021.116930, URL https://doi.org/10.1016/j.actamat.2021.116930https://linkinghub.elsevier.com/retrieve/pii/S1359645421003104.

[55] Y. Lian, S. Lin, W. Yan, W.K. Liu, G.J. Wagner, A parallelized three-dimensional cellular automaton model for grain growth during additive manufacturing, Comput. Mech. 61 (5) (2018) 543–558, http://dx.doi.org/10.1007/s00466-017-1535-8, URL https://doi.org/10.1007/s00466-017-1535-8http://link.springer.com/10.1007/s00466-017-1535-8.

[56] M. Rolchigo, B. Stump, J. Belak, A. Plotkowski, Sparse thermal data for cellular automata modeling of grain structure in additive manufacturing, Modelling Simul. Mater. Sci. Eng. 28 (6) (2020) http://dx.doi.org/10.1088/1361-651X/ab9734.

[57] O. Zinovieva, A. Zinoviev, V. Romanova, R. Balokhonov, Three-dimensional analysis of grain structure and texture of additively manufactured 316L austenitic stainless steel, Addit. Manuf. 36 (July) (2020) 101521, http://dx.doi.org/10.1016/j.addma.2020.101521.

[58] J.G. Pauza, W.A. Tayon, A.D. Rollett, Computer simulation of microstructure development in powder-bed additive manufacturing with crystallographic texture, Modelling Simul. Mater. Sci. Eng. 29 (5) (2021) http://dx.doi.org/10.1088/1361-651X/ac03a6.

[59] W. Li, M. Soshi, Modeling analysis of the effect of laser transverse speed on grain morphology during directed energy deposition process, Int. J. Adv. Manuf. Technol. 103 (9–12) (2019) 3279–3291, http://dx.doi.org/10.1007/s00170-019-03690-6, URL http://link.springer.com/10.1007/s00170-019-03690-6.

[60] T.M. Rodgers, J.D. Madison, V. Tikare, Simulation of metal additive manufacturing microstructures using kinetic Monte Carlo, Comput. Mater. Sci. 135 (2017) 78–89, http://dx.doi.org/10.1016/j.commatsci.2017.03.053, arXiv:NIHMS150003, URL http://dx.doi.org/10.1016/j.commatsci.2017.03.053https://linkinghub.elsevier.com/retrieve/pii/S0927025617301751.

[61] V. Attari, P. Honarmandi, T. Duong, D.J. Sauceda, D. Allaire, R. Arroyave, Uncertainty propagation in a multiscale CALPHAD-reinforced elastochemical phase-field model, Acta Mater. 183 (2020) 452–470, http://dx.doi.org/10.1016/j.actamat.2019.11.031, arXiv:1908.00638.

[62] A.F. Chadwick, P.W. Voorhees, The development of grain structure during additive manufacturing, Acta Mater. 211 (2021) 116862, http://dx.doi.org/10.1016/j.actamat.2021.116862.

[63] K. Karayagiz, L. Johnson, R. Seede, V. Attari, B. Zhang, X. Huang, S. Ghosh, T. Duong, I. Karaman, A. Elwany, R. Arróyave, Finite interface dissipation phase field modeling of Ni–Nb under additive manufacturing conditions, Acta Mater. 185 (2020) 320–339, http://dx.doi.org/10.1016/j.actamat.2019.11.057, arXiv:1906.10200, URL https://linkinghub.elsevier.com/retrieve/pii/S1359645419307979.

[64] T. Keller, G. Lindwall, S. Ghosh, L. Ma, B.M. Lane, F. Zhang, U.R. Kattner, E.A. Lass, J.C. Heigel, Y. Idell, M.E. Williams, A.J. Allen, J.E. Guyer, L.E. Levine, Application of finite element, phase-field, and CALPHAD-based methods to additive manufacturing of Ni-based superalloys, Acta Mater. 139 (2017) 244–253, http://dx.doi.org/10.1016/j.actamat.2017.05.003, arXiv:1705.02016.

[65] L.X. Lu, N. Sridhar, Y.W. Zhang, Phase field simulation of powder bed-based additive manufacturing, Acta Mater. 144 (2018) 801–809, http://dx.doi.org/10.1016/j.actamat.2017.11.033.

[66] Z. Zhang, X.X. Yao, P. Ge, Phase-field-model-based analysis of the effects of powder particle on porosities and densities in selective laser sintering additive manufacturing, Int. J. Mech. Sci. 166 (July 2019) (2020) http://dx.doi.org/10.1016/j.ijmecsci.2019.105230.

[67] K. Teferra, L. Graham-Brady, Tessellation growth models for polycrystalline microstructures, Comput. Mater. Sci. 102 (2015) 57–67, http://dx.doi.org/10.1016/j.commatsci.2015.02.006.

[68] R. Saunders, C. Butler, J. Michopoulos, D. Lagoudas, A. Elwany, A. Bagchi, Mechanical behavior predictions of additively manufactured microstructures using functional Gaussian process surrogates, Npj Comput. Mater. 7 (1) (2021) 81, http://dx.doi.org/10.1038/s41524-021-00548-y, URL http://dx.doi.org/10.1038/s41524-021-00548-yhttp://www.nature.com/articles/s41524-021-00548-y.

[69] B. Zhang, R. Seede, L. Xue, K.C. Atli, C. Zhang, A. Whitt, I. Karaman, R. Arroyave, A. Elwany, An efficient framework for printability assessment in Laser Powder Bed Fusion metal additive manufacturing, Addit. Manuf. 46 (June) (2021) 102018, http://dx.doi.org/10.1016/j.addma.2021.102018, URL https://doi.org/10.1016/j.addma.2021.102018https://linkinghub.elsevier.com/retrieve/pii/S2214860421001834.

[70] S.A. Khairallah, A.A. Martin, J.R. Lee, G. Guss, N.P. Calta, J.A. Hammons, M.H. Nielsen, K. Chaput, E. Schwalbach, M.N. Shah, M.G. Chapman, T.M. Willey, A.M. Rubenchik, A.T. Anderson, Y. Morris Wang, M.J. Matthews, W.E. King, Controlling interdependent meso-nanosecond dynamics and defect generation in metal 3D printing, Science 368 (6491) (2020) 660–665, http://dx.doi.org/10.1126/science.aay7830.

[71] Z. Feng, R. Pokharel, S.C. Vogel, R.A. Lebensohn, D. Pagan, E. Zepeda-Alarcon, B.r. Clausen, R. Martinez, G.T. Gray, M. Knezevic, Crystal plasticity modeling of strain-induced martensitic transformations to predict strain rate and temperature sensitive behavior of 304 L steels: Applications to tension, compression, torsion, and impact, Int. J. Plast. 156 (April) (2022) http://dx.doi.org/10.1016/j.ijplas.2022.103367.

[72] J. Ye, M. Mahmoudi, K. Karayagiz, L. Johnson, R. Seede, I. Karaman, R. Arroyave, A. Elwany, Bayesian calibration of multiple coupled simulation models for metal additive manufacturing: A Bayesian network approach, ASCE-ASME J. Risk Uncert Eng. Syst. B Mech. Eng. 8 (1) (2022) 1–12, http://dx.doi.org/10.1115/1.4052270, URL https://asmedigitalcollection.asme.org/risk/article/8/1/011111/1119199/Bayesian-Calibration-of-Multiple-Coupled.

[73] C.E. Rasmussen, C.K.I. Williams, Regression, in: Gaussian Processes for Machine Learning, The MIT Press, 2005, http://dx.doi.org/10.7551/mitpress/3206.003.0005, URL https://direct.mit.edu/books/book/2320/chapter/60736/regression.

[74] M. Kennedy, Predicting the output from a complex computer code when fast approximations are available, Biometrika 87 (1) (2000) 1–13, http://dx.doi.org/10.1093/biomet/87.1.1, URL https://academic.oup.com/biomet/article-lookup/doi/10.1093/biomet/87.1.1.

[75] D. Higdon, J. Gattiker, B. Williams, M. Rightley, Computer model calibration using high-dimensional output, J. Amer. Statist. Assoc. 103 (482) (2008) 570–583, http://dx.doi.org/10.1198/016214507000000888, URL https://www.tandfonline.com/doi/full/10.1198/016214507000000888.

[76] M. Mahmoudi, G. Tapia, K. Karayagiz, B. Franco, J. Ma, R. Arroyave, I. Karaman, A. Elwany, Multivariate calibration and experimental validation of a 3D finite element thermal model for laser powder bed fusion metal additive manufacturing, Integr. Mater. Manuf. Innov. (ISSN: 2193-9764) 7 (3) (2018) 116–135, http://dx.doi.org/10.1007/s40192-018-0113-z, arXiv:2187373, URL http://link.springer.com/10.1007/s40192-018-0113-z.

[77] P. Perdikaris, M. Raissi, A. Damianou, N.D. Lawrence, G.E. Karniadakis, Nonlinear information fusion algorithms for data-efficient multi-fidelity modelling, Proc. R. Soc. A: Math., Phys. Eng. Sci. 473 (2198) (2017) http://dx.doi.org/10.1098/rspa.2016.0751.

[78] M.A. Álvarez, L. Rosasco, N.D. Lawrence, Kernels for vector-valued functions: A review, Found. Trends® Mach. Learn. 4 (3) (2012) 195–266, http://dx.doi.org/10.1561/2200000036, arXiv:arXiv:1106.6251v2 URL http://www.nowpublishers.com/article/Details/MAL-036.

[79] B. Wang, A. Xu, Gaussian process methods for nonparametric functional regression with mixed predictors, Comput. Stat. Data Anal. 131 (2019) 80–90, http://dx.doi.org/10.1016/j.csda.2018.07.009, URL https://doi.org/10.1016/j.csda.2018.07.009https://linkinghub.elsevier.com/retrieve/pii/S0167947318301750.